Elucidating the characteristic energy balance evolution in applied smouldering systems

Energy 273 (2023) 127245

Contents lists available at ScienceDirect

Energy

journal homepage: www.elsevier.com/locate/energy

Elucidating the characteristic energy balance evolution in applied smouldering systems

Tarek L. Rashwan [a,b,c,*], Marco A.B. Zanoni [a], Jiahao Wang [a], José L. Torero [d], Jason I. Gerhard [a,‡]

[a] Department of Civil and Environmental Engineering, The University of Western Ontario, London, Ontario, N6A 5B9, Canada
[b] Department of Civil Engineering, Lassonde School of Engineering, York University, Toronto, Ontario, M3J 1P3, Canada
[c] School of Engineering & Innovation, The Open University, Milton Keynes, MK7 6AA, UK
[d] Department of Civil, Environmental and Geomatic Engineering, University College London, London, WC1E 6BT, UK

ARTICLE INFO

Handling Editor: L Luo

Keywords:
Smouldering combustion
Local thermal non-equilibrium
Steady state
Heat losses
Porous media
Process scale-up

ABSTRACT

Applied smouldering systems are emerging to solve a range of environmental challenges, such as remediation, sludge treatment, off-grid sanitation, and resource recovery. In many cases, these systems use smouldering to drive an efficient waste-to-energy process. While engineers and researchers are making strides in developing these systems, the characteristic energy balance trends have not yet been well-defined. This study addresses this topic and presents a detailed framework to uncover the characteristic energy balance evolution in applied smouldering systems. This work provides new experimental results; a new, validated analytical description of the cooling zone temperature profile at steady-state conditions; insight into the characteristic temperature changes over time; a re-analysis of published data; and a robust framework to contextualize the global energy balance results from applied smouldering systems. Altogether, this study is aimed to support researchers and engineers to better understand smouldering system performance to further the development of environmentally beneficial applications.

1. Introduction

There has been a recent flurry of research and commercial activity as applied smouldering systems are being developed to tackle a growing range of environmental challenges, e.g., for (*i*) contaminated land remediation [1,2], (*ii*) hazardous waste treatment [3,4], (*iii*) resource generation and recovery [5–9], (*iv*) pyrolysis/torrefaction [10–13], (*v*) off-grid sanitation [14,15], (*vi*) food waste disposal [16], and (*vii*) wastewater sludge treatment [17–19]. In these cases, smouldering has unique benefits opposed to other thermal conversion options (e.g., flaming-based incinerators). For example, smouldering systems can operate in a self-sustaining manner using wastes with low volatility (e.g., oil sludges and waste heavy hydrocarbons [3,20,21]) and/or high moisture content (MC) (e.g., 74% MC faeces [22], 80% MC sewage sludge [23], and 85% MC anaerobic digestate [24]). Numerous studies have also explored: (*i*) scaling-up applied smouldering systems [18,25–29] (where applications are now commercialized [1,30–32]), (*ii*) various reactor configurations for continuous operation [9,18,33–36], (*iii*) soil changes upon smouldering [37,38], (*iv*) treating and understanding hazardous emissions [39–41], and (*v*) energy recovery [10,32,42,43] (including from large, naturally occurring smouldering coal-field fires [44,45]). Altogether, smouldering systems present strong potential as a novel and sustainable waste-to-energy technique that is highly compatible within a circular economy [5,30,46].

Smouldering is a flameless form of combustion driven as oxygen in the pore-space transports to the surface of the fuel and then reacts [46,47]. Smouldering can be self-sustaining so long as the energy released rate overwhelms local heat losses rate (e.g., due to heating nearby fuel, phase change processes, endothermic reactions) [46,48–50]. Beyond the pore-scale, smouldering is characterized by a series of zones that evolve throughout space and time. Fig. 1 presents a conceptual model of these zones in an applied smouldering system, along with a common centre-line temperature profile and a picture of an oil-drum sized reactor (DRUM). These systems often use wastes mixed within inert porous media (e.g., silica sand) to provide the necessary mixture conditions for smouldering, e.g., (*i*) permeable pathway for oxygen, (*ii*) sufficiently high specific surface area, and (*iii*) energy recycling between the sand,

* Corresponding author. School of Engineering & Innovation, The Open University, Milton Keynes, MK7 6AA, UK.
E-mail addresses: tarek.rashwan@open.ac.uk (T.L. Rashwan), mbazelat@uwo.ca (M.A.B. Zanoni), jwan753@uwo.ca (J. Wang), j.torero@ucl.ac.uk (J.L. Torero).
‡ Deceased.

https://doi.org/10.1016/j.energy.2023.127245
Received 22 October 2022; Received in revised form 14 February 2023; Accepted 17 March 2023
Available online 22 March 2023

Nomenclature

Abbreviations

CEMS	Continuous emissions measurement system
DT	Dimensionless time
DRUM	Oil-drum sized reactor (0.300 m radius)
GAC	Granular activated carbon
IPM	Inert porous media
LAB	Large laboratory reactor (0.080 m radius)
LAB2	Small laboratory reactor (0.054 m radius)
LTNE	Local thermal non-equilibrium
MC	Moisture content (wet mass basis)

Latin Letters

a_{sg}	Specific surface area, m^{-1}
A	Cross-sectional area, m^2
C_p	Specific heat capacity, J kg^{-1} K^{-1}
d_p	Particle diameter, m
E	Energy, J
E_{net}/A	Net stored energy per cross-sectional area at the centreline, J m^{-2}
$\dot{E}$	Energy rate, J s^{-1}
$\overline{E}$	Dimensionless energy
fr_{CO}	Fraction of carbon oxidized to carbon monoxide
h	Heat transfer coefficient, W m^{-2} K^{-1}
h_{sg}	Interfacial heat transfer coefficient, W m^{-2} K^{-1}
H	Modified heat transfer coefficient, m^{-1}
J_a	the Bessel function of the first kind
k	Thermal conductivity, W m^{-1} K^{-1}
l	Length, m
L	Dimensionless length
m/m	Mass fraction
$C_p\dot{m}''$	Heat capacity rate flux, J m^{-2} s^{-1} K^{-1}
Nu	Nusselt Number
Pe	Peclet Number
Pr	Prandtl number
Re	Reynold's number
r_o	Outer radius, m
R	Dimensionless outer radius
t_c	Characteristic time, s
T_{peak}	Maximum temperature, K
T_{amb}	Ambient temperature, K
u_g	Darcy flux, m s^{-1}
U	Global heat loss coefficient, W m^{-2} K^{-1}
v_{oxid}	Smouldering velocity, m s^{-1}
v_{cool}	Cooling velocity, m s^{-1}
x_c	Characteristic distance, m
$\widehat{x}$	Transformed distance, m

Greek Symbols

α_I	Dimensionless modified heat transfer coefficient (Hr_o)
α_{II}	Dimensionless modified heat transfer coefficient (Hx_c)
γ_m	Positive root from a transcendental equation
δ	Small dimensionless interfacial heat transfer parameter
λ_I	Dimensionless constant (1)
λ_{II}	Dimensionless constant (2)
μ	Dynamic viscosity, Pa·s
ξ	Dimensionless distance
ρ	Density, kg m^{-3}
σ	Stephan Boltzmann constant, W m^{-2} K^{-4}
τ	Dimensionless time
φ	Porosity
$\Delta\xi$	Difference between dimensionless distances
$\Delta\theta$	Dimensionless difference between gas and solid temperatures
ΔH_{oxid}	Heat of smouldering, MJ kg^{-1}

Subscripts

0	Initial
amb	Ambient
app	Approximate
bulk	Volume averaged
c	Characteristic
cool	Cooling
crit	Critical
eff	Effective
f	Final
g	Gas/air
ig	Ignition
in	Into control volume
ins	Insulation
loss	Lost from control volume
net	Net stored
out	Out of control volume
oxid	Oxidation
pyr	Pyrolysis
r	Radial
s	Solid/sand
vap	Vaporization
x	Axial

air, and fuel [23,46,51].

The zones in Fig. 1 are common to smouldering systems, i.e., the *cooling*, *reaction*, and *inert heating zones*. The reaction zone is the driving force that delineates all chemical reactions, i.e., exothermic reactions (primarily fuel oxidation) and endothermic reactions (primarily pyrolysis) [46]. Though these reactions may compete throughout space, pyrolysis generally precedes oxidation [52,53]. Ahead of the reactions, the energy evolved from smouldering drives fuel preheating and phase change processes (e.g., boiling/evaporation [54]) in the inert heating zone. Behind the reactions, the remaining hot inert material is cooled by the incoming applied air and perimeter heat losses [29,55]. The heat transfer in this zone is fundamentally driven by local thermal non-equilibrium (LTNE) [29,56–58].

While Fig. 1 illustrates there are multiple dynamic processes that evolve in smouldering systems throughout space, it is also useful to consider the energy balance around the entire system, i.e., the *global energy balance*. Equation (1) presents the key global energy balance terms that govern the waste-to-energy potential of smouldering systems [48,59]:

$$\frac{dE_{net}}{dt}(t) = \dot{E}_{in}(t) + \dot{E}_{oxid}(t) - \dot{E}_{pyr}(t) - \dot{E}_{loss}(t) - \dot{E}_{out}(t) \quad (1)$$

where $\dot{E}_{in}$ and $\dot{E}_{out}$ are the rates of energy added for ignition and lost primarily via convection upon smouldering completion, respectively; $\dot{E}_{oxid}$ and $\dot{E}_{pyr}$ are the rates that energy is chemically released (from exothermic reactions, primarily oxidation) and absorbed (from endothermic reactions, primarily pyrolysis), respectively; $\dot{E}_{loss}$ is the rate of energy lost as perimeter heat losses; and dE_{net}/dt is the net rate of energy accumulation in the system. Note that $\dot{E}_{in}$ and $\dot{E}_{out}$ only represent initial- and end-effects, respectively, and can be neglected throughout most of smouldering propagation [27,29]. In addition, the pyrolysis effects are often small in robust applied smouldering systems, e.g., using bitumen [48,59]. Alternatively, the net effect of $\dot{E}_{pyr}$ and $\dot{E}_{loss}$ can often be

combined into an 'effective' source term in applied smouldering systems where these reactions travel close together [46,60]. Therefore, the dE_{net}/dt in applied smouldering systems is often governed by the balance between $\dot{E}_{oxid}$ (or an effective source term) and $\dot{E}_{loss}$ [27,29]. Note that Eq. (1) does not account for energy lost due to water evaporation, but it could be included [54].

In addition, it is useful to examine the terms from Eq. (1) integrated over time, i.e., $E = \int_0^t \dot{E}dt$. For example, the energy accumulated in smouldering systems, E_{net}, is solved by either balancing all terms in Eq. (1) and integrating over time, or integrating temperatures throughout time and space [27,29]:

$$E_{net}(t) = \iiint_V \int_{T_{amb}}^{T_s(x,r,t)} (1-\varphi)\rho_s C_{p_s}(T_s) dTdV \; for \; 0 < t \tag{2}$$

Torero et al. [46], recently provided an overview of smouldering energy balance developments, which is summarized below. The smouldering front characteristics ultimately result from a *local energy balance*, i.e., only within the reaction zone, which was resolved by many researchers using traditional combustion analyses, e.g., by Dosanjh et al. [61] and Aldushin et al. [62]. However, the local energy balance in smouldering systems often relies on dynamic inputs that need to be resolved across the entire system, i.e., using a global energy balance [46]. Zanoni et al. [48,59], provided a numerical modelling approach to resolve the terms from Eq. (1) both globally and locally. A major advantage of this approach is that it provided insight into the dynamic evolution of smouldering systems and the impacts of system input changes on smouldering performance. For example, Torero et al. [46], provides examples that demonstrate how global and local energy balance results can together predict system quenching and the influence of interventions to maintain self-sustaining smouldering. Multiple recent studies have since extended the insights from Zanoni et al. [48,59], to better understand many phenomena, e.g., (*i*) limits of ignition/extinction [50,63,64] (*ii*) sensitivities to key operating parameters (e.g., fuel concentration, and air flux) [10,65], and (*iii*) system energy efficiency gains with scale [27,29]. However, many of these studies have focused on smouldering characteristics that were far from global steady-state conditions, and few studies have pursued steady-state analyses.

Fig. 2 presents numerical modelling results from Zanoni et al. [48], which resolved all terms from Eq. (1), as an example to demonstrate key global energy balance changes over time common to applied smouldering systems. Moreover, this figure provides modelling data that simulates smouldering system behaviour in a large domain that facilitated effective global steady-state conditions (note that these model results are re-analyzed in Section 3 as LAB B1 – see Table 1). Fig. 2a shows the temperature-time profiles from the simulation, Fig. 2b shows the evolutions of the terms on the righthand side of Eq. (1) resolved over the entire system, and Fig. 2c shows the evolutions of the balance of all terms in Fig. 2b (i.e., rate of net stored energy, black curve) and the net stored energy (i.e., red curve). As mentioned above, Fig. 2b shows that $\dot{E}_{in}$ and $\dot{E}_{out}$ were indeed initial- and end-effects, respectively, and $\dot{E}_{pyr}$ was minimal. Therefore, $\dot{E}_{oxid}$ and $\dot{E}_{loss}$ governed the energy balance. That is, the system initially accumulated large amounts of energy in the 'early, transient times' as $\dot{E}_{oxid} > \dot{E}_{loss}$. However, while $\dot{E}_{oxid}$ was nearly constant, $\dot{E}_{loss}$ increased over time and drew more energy from the system as the cooling zone grew and provided a longer region for heat losses. Therefore, at 'late, steady times', $\dot{E}_{loss}$ approximately balanced $\dot{E}_{oxid}$ and the system approached a steady-state condition. Towards steady-state conditions, the net stored energy approached a maximum, constant value (i.e., E_{net}, seen as the red line in Fig. 2c). Note that nearly all stored energy accumulates in the cooling zone in applied smouldering systems [29,65]. While Fig. 2 demonstrates this transition to steady-state conditions, no study has yet generalized the conditions that govern the characteristic energy evolution of smouldering systems.

This study presents a framework to describe the characteristic evolution of the global energy balance common to applied smouldering systems. This was achieved by deriving a new analytical model of the steady-state temperature profile throughout the cooling zone – which accounts for nearly all stored energy – to approximately define the maximum amount of stored energy. This framework was applied to a validated numerical model and experiments under various conditions (e.g., reactor width, fuel type, fuel concentration, insulation quality, and air flux). The results were made non-dimensional and shown to collapse onto a unified curve, which demonstrates the characteristic global energy balance evolution. Altogether, this analysis elucidates the key influences on the global energy balance, which can be manipulated by engineers in designing smouldering systems for environmentally beneficial purposes.

2. Methodology

2.1. Expressing the energy balance with non-dimensional terms

To develop a characteristic energy balance curve, the transient net stored energy (E_{net}) and time (t) need to be expressed non-dimensionally. The energy needs to be non-dimensional ($\overline{E}_{net}$) to the maximum stored energy at steady-state conditions, i.e., $E_{net,f}$ when $\dot{E}_{oxid} \approx \dot{E}_{loss}$ in Eq. (1) [29,48,60], and the time needs to be non-dimensional (τ) to the approximate time required to reach this condition (t_f). These terms also need to account for the ignition effects and can be described as:

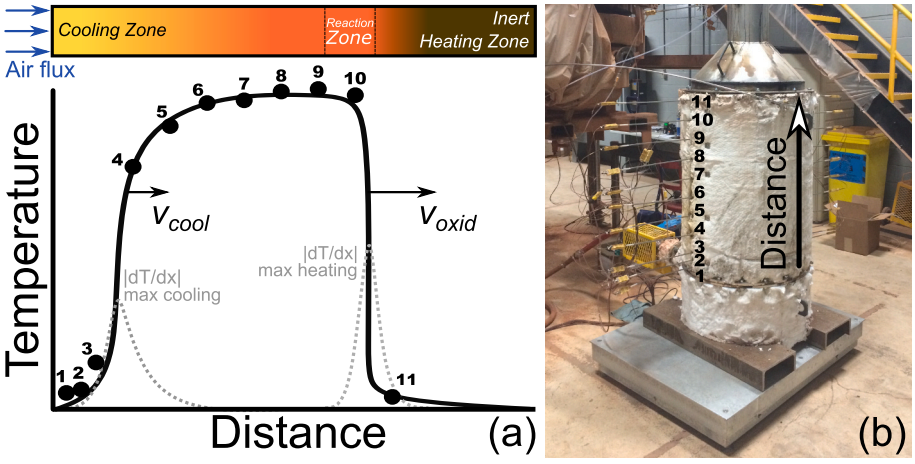

Fig. 1. (a) Conceptual model of the temperature distribution through the centreline of a smouldering system (solid line), overlain with temperature data (markers) from the end of propagation through a 0.9 m tall mixture of granular activated carbon and coarse grain sand (i.e., the end profile of DRUM R2, detailed in Table 1). The key zones: *Inert Heating Zone*, *Reaction Zone*, and *Cooling Zone* are highlighted for further discussion and are approximately bounded between the velocities of the smouldering front (v_{oxid}) and the cooling front (v_{cool}), where $v_{oxid} > v_{cool}$. (b) A picture of the oil-drum sized reactor (DRUM) used to conduct the experiment plotted in (a).

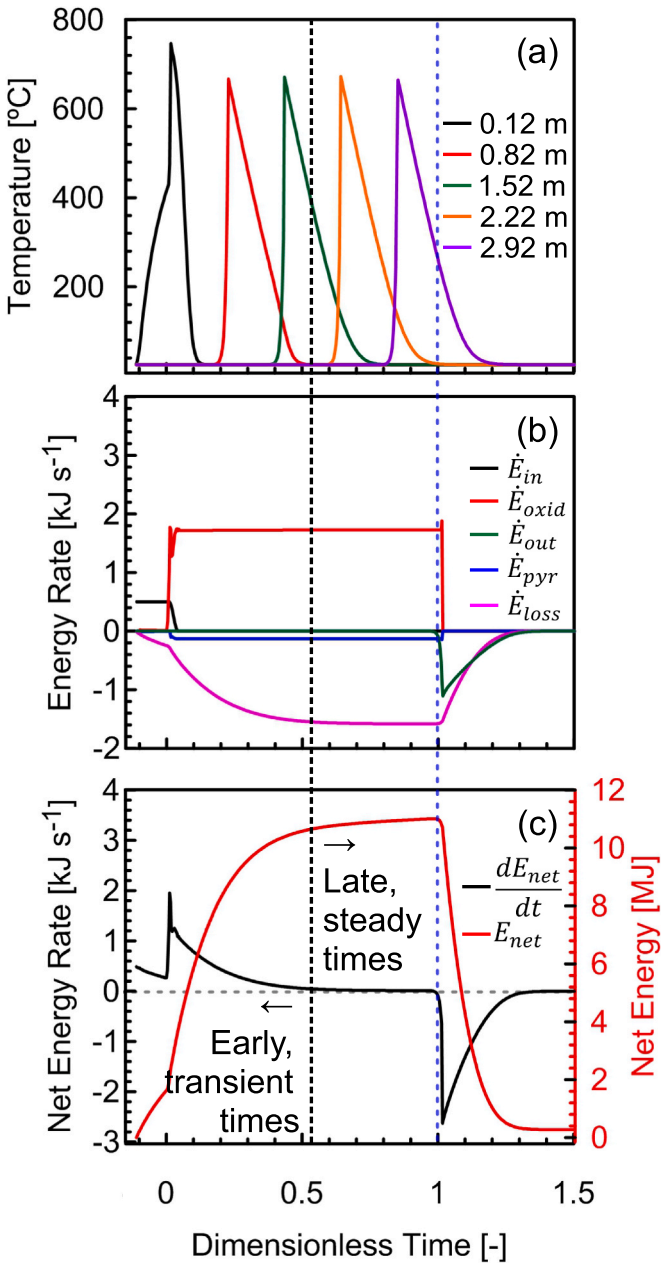

Fig. 2. LAB B1 numerical modelling results from Ref. [48] that show: (a) temperatures, (b) the terms global energy balance terms from the righthand side of Eq. (1), and (c) the balance of Eq. (1) terms (dE_{net}/dt) and the net stored energy (E_{net}). The profiles in (a–c) are normalized over dimensionless time (DT) [66], where DT = 0 notes ignition and DT = 1 notes the end of propagation (i.e., when the smouldering front reached the end of the fuel bed, which is marked in (a–c) with a dashed blue vertical line). The horizontal dashed grey line in (c) notes $\dot{E}_{net} = 0$ and the dashed vertical black line in (a–c) approximately shows when $\dot{E}_{loss}(t) = 0.9\dot{E}_{oxid}(t)$ (i.e., when the front propagated around 1.6 m just after $DT = 0.5$). The black vertical line delineates the 'early, transient times' from the 'late, steady times'. This figure was adapted from Refs. [29,48], with permission of Elsevier. (For interpretation of the references to colour in this figure legend, the reader is referred to the Web version of this article.)

$$\tau = \frac{t - t_{ig}}{t_f}; t_f = \frac{l_{cool,f} - l_{ig}}{v_{oxid} - v_{cool}} \tag{3}$$

$$\overline{E}_{net} = \frac{E_{net} - E_{net,ig}}{E_{net,f} - E_{net,ig}} \tag{4}$$

where t_{ig} is the ignition time (i.e., identified as when the heater was turned off), l_{ig} is the heated length upon ignition, $l_{cool,f}$ is the steady-state cooling length, v_{oxid} is the smouldering velocity, v_{cool} is the cooling velocity [67], and $E_{net,ig}$ is the stored energy accumulated prior to ignition. In convective and radiative ignition systems, l_{ig} equals the smouldering distance upon ignition; in conductive ignition systems, l_{ig} equals the smouldering distance plus the hot sand below the heater element upon ignition (which was approximately 0.1 m in LAB S1 and B1). In all cases, the l_{ig} and $l_{cool,f}$ terms represent approximate lengths of hot regions. Because nearly all the stored energy in applied smouldering systems using inert media accumulate in the reaction-less cooling zone [29,59], this zone was targeted to estimate the terms in Eqs. (3) and (4).

2.2. Estimating $E_{net,f}$ from a steady-state profile

To estimate $E_{net,f}$, a new analytical solution was developed to describe this temperature field throughout the cooling zone based on the system and smouldering conditions. That is, the temperatures throughout the reaction and preheating zones were not modelled. This formulation followed the perturbation method from Kuznetsov [67,68] for local thermal non-equilibrium (LTNE) heat transfer between the gas (air) and solid (sand) phases and fixed the frame of reference to the smouldering front (i.e., common to smouldering analyses [58,61,62,69]).

The cooling zone was idealized as a 2D cylindrical system using volume-averaged energy equations for the air and solid phases [70]:

$$\varphi\rho_g C_{p_g}\frac{\partial T_g}{\partial t} + \rho_g C_{p_g} u_g \frac{\partial T_g}{\partial x} = \varphi k_g\left[\frac{\partial^2 T_g}{\partial x^2} + \frac{\partial^2 T_g}{\partial r^2} + \frac{1}{r}\frac{\partial T_g}{\partial r}\right] + h_{sg}a_{sg}\left(T_s - T_g\right) \tag{5}$$

$$(1-\varphi)\rho_s C_{p_s}\frac{\partial T_s}{\partial t} = (1-\varphi)k_{s_{app}}\left[\frac{\partial^2 T_s}{\partial x^2} + \frac{\partial^2 T_s}{\partial r^2} + \frac{1}{r}\frac{\partial T_s}{\partial r}\right] - h_{sg}a_{sg}\left(T_s - T_g\right) \tag{6}$$

where radiation heat transfer was embedded in the solid conductivity following the Rosseland approximation, $k_{s_{app}} = k_s + 16\sigma d_p T_s^3/3$ [56], and the specific surface area was estimated assuming the sand grains were spherical, $a_{sg} = 6(1-\varphi)/d_p$ [56,70]. While there are multiple correlations available to estimate LTNE heat transfer (e.g. Refs. [71,72]), the interfacial heat transfer coefficient (h_{sg}) was approximated following Zanoni et al. [56], as it has been shown to accurately capture LTNE heat transfer in smouldering systems [12,29,57–59,64,73]:

$$Nu = h_{sg}d_p / k_g = 0.001\left(Re^{1.97}\,\mathrm{Pr}^{1/3}\right) \tag{7}$$

Equation (7) is valid for $Pr = 0.72$, $0.5 \le Re \le 31$, and $0.125 \le d_p \le 2.000$ mm [56].

Equations (5) and (6), were then transformed by fixing the frame of reference on the smouldering front, as the cooling zone was assumed to be fixed relative to the smouldering front, i.e., $\hat{x} = x - v_{oxid}t$ [58]. The transient term is then dropped to focus on steady-state cooling zone characteristics upstream of the smouldering front:

$$\rho_g C_{p_g}\left(u_g - \varphi v_{oxid}\right)\frac{\partial T_g}{\partial \hat{x}} = \varphi k_g\left[\frac{\partial^2 T_g}{\partial \hat{x}^2} + \frac{\partial^2 T_g}{\partial r^2} + \frac{1}{r}\frac{\partial T_g}{\partial r}\right] + h_{sg}a_{sg}\left(T_s - T_g\right) \tag{8}$$

Table 1
Experimental conditions and key smouldering front results.

Experimental Conditions				[a] Smouldering Front Results			
Experiment and Reference	Fuel/sand (g_{fuel} kg_s^{-1}) LAB ± 0.3% DRUM ± 2%	[b] Darcy air flux (cm s^{-1}) LAB ± 3% DRUM ± 2%	Initial fuel bed height (m) ±0.003 m	Borderline-/Self-sustaining? (BSS/SS)	Mean propagation velocity (cm min^{-1}) LAB ± 4% DRUM ± 10%	Mean peak temperature (°C) LAB ± 1% DRUM ± 4%	[c] Mean fr_{CO} LAB ± 10% DRUM ± 2%
Experimental Results							
DRUM R0 [27]	20.0	5.0	0.813	SS	0.46	804	-[d]
DRUM R1 [27]	20.0	7.5	0.868	SS	0.47	765	-[d]
DRUM R2 [27]	23.3	5.0	0.865	SS	0.44	834	-[d]
LAB R1 [27]	20.0	7.5	0.568	SS	0.61	766	0.27
LAB R2 [27]	23.3	5.0	0.560	SS	0.49	874	0.27
LAB2 R0a [73]	20.0	5.0	0.735	SS	0.42	655	0.28
LAB2 R0b [73]	20.0	5.0	0.735	SS	0.34	640	0.26
LAB S1	222	3.3	1.135	BSS	0.29	530	0.12
Numerical Result							
LAB B1 [48]	34.2	5.8	3.000	SS	0.42	679	-[e]

Experimental Conditions' errors represent conservative estimates of experimental equipment error. *Smouldering Front Results*' errors are conservative estimates of experimental variability and are normalized standard deviations from three DRUM and LAB repeat experiments from smouldering wastewater sewage sludge. These errors align well with similar experimental studies [23,57,66,81,82]. The LAB errors are representative of the LAB2 systems, which used the same equipment except a different sized reactor.

[a] The smouldering front metrics capture smouldering conditions sufficiently far from ignition and end effects [27].
[b] At standard temperature and pressure (21.1 °C at 1 atm).
[c] The percentages represent volume fractions and $fr_{CO} = CO\% / (CO\% + CO_2\%)$.
[d] CO measurement throughout propagation exceeded DRUM emissions analyzer calibration range, i.e., 0–0.3 vol%.
[e] CO production was not simulated.

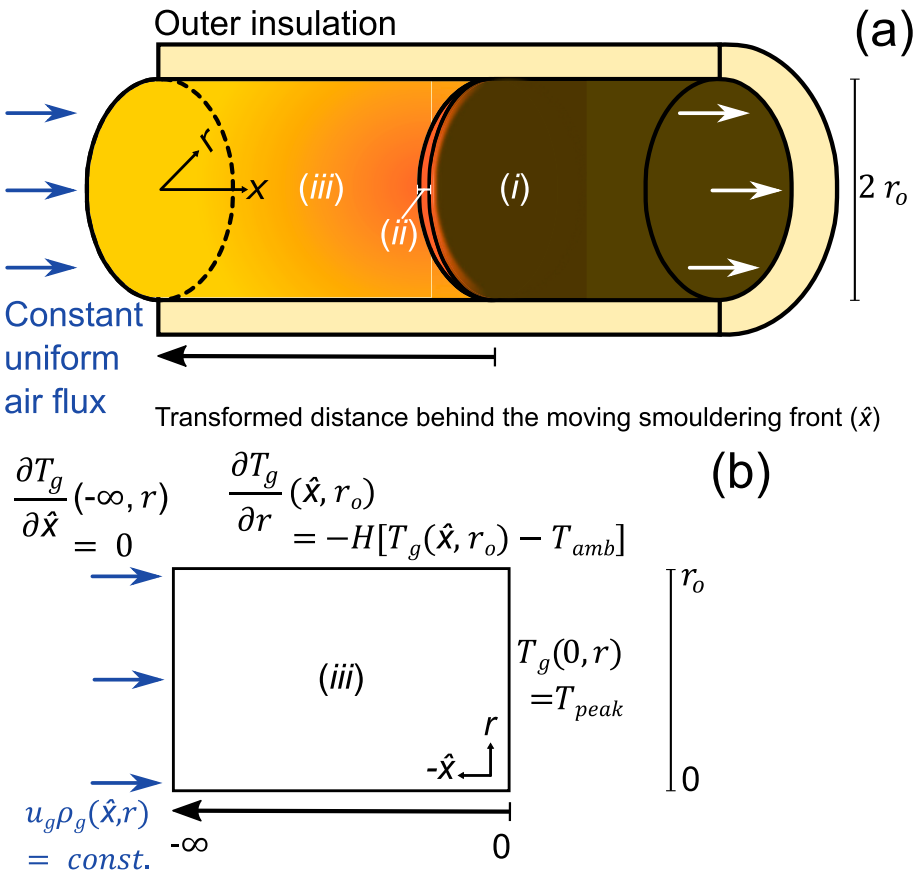

Fig. 3. (a) Schematic of the smouldering system where (*i*), (*ii*), and (*iii*) show the *Inert Heating Zone*, *Reaction Zone* and *Cooling Zone*, respectively; and (b) a simplified conceptual model with the boundary conditions used to solve the temperature profile within the cooling zone. This figure was adapted from a similar schematic in Rashwan et al., [29], with permission of Elsevier.

$$-\rho_s C_{p_s} v_{oxid}(1-\varphi)\frac{\partial T_s}{\partial \hat{x}} = (1-\varphi)k_{s_{app}}\left[\frac{\partial^2 T_s}{\partial \hat{x}^2}+\frac{\partial^2 T_s}{\partial r^2}+\frac{1}{r}\frac{\partial T_s}{\partial r}\right] - h_{sg}a_{sg}\left(T_s - T_g\right) \tag{9}$$

Equations (8) and (9) were then made non-dimensional following simplifications and non-dimensional descriptions:

$$\theta = \frac{(T-T_{amb})}{\left(T_{peak}-T_{amb}\right)}, \xi_r = \frac{r}{r_o}, \xi_x = \frac{\hat{x}k_{bulk}}{r_o^2 C_p \dot{m}''_{bulk}} \tag{10}$$

$$\delta = \frac{k_{bulk}}{r_o^2 h_{sg} a_{sg}}, \theta_s = \theta_g + \delta\Delta\theta \tag{11}$$

where $\rho_g C_{p_g}(u_g - \varphi v_{oxid}) = C_p \dot{m}''_g$, $\rho_s C_{p_s} v_{oxid}(1-\varphi) = C_p \dot{m}''_s$, $C_p \dot{m}''_g - C_p \dot{m}''_s = C_p \dot{m}''_{bulk}$, and $\varphi\rho_g C_{p_g} + (1-\varphi)\rho_s C_{p_s} = (\rho C_p)_{bulk}$, $\varphi k_g + (1-\varphi)k_{s_{app}} = k_{bulk}$. Note that $C_p \dot{m}''_{bulk}$ is a negative value under the conditions investigated, as $C_p \dot{m}''_s > C_p \dot{m}''_g$. Furthermore, δ was defined as very small parameter to permit the perturbation analysis [67,68]; therefore, the perturbation analysis is invalid at small reactor radii, i.e., $\lesssim O$ (0.01 m). Equations (8) and (9) then become:

$$\frac{\partial \theta_g}{\xi_x} = \frac{1}{\xi_r}\frac{\partial}{\partial \xi_r}\left(\xi_r \frac{\partial \theta_g}{\partial \xi_r}\right) + \frac{1}{Pe_{eff}^2}\frac{\partial^2 \theta_g}{\partial \xi_x^{\,2}} + O(\delta) \tag{12}$$

$$\Delta\theta = \lambda_I \frac{\partial \theta_g}{\xi_x} - \lambda_{II}\left[\frac{1}{\xi_r}\frac{\partial}{\partial \xi_r}\left(\xi_r \frac{\partial \theta_g}{\partial \xi_r}\right)\right] + \frac{1}{Pe_{eff}^2}\frac{\partial^2 \theta_g}{\partial \xi_x^{\,2}} \tag{13}$$

where $\lambda_I = C_p \dot{m}''_g / C_p \dot{m}''_{bulk}$, $\lambda_{II} = \varphi k_g / k_{bulk}$, and $Pe_{eff} = r_o C_p \dot{m}''_{bulk} / k_{bulk}$.

The following boundary conditions were then applied to Eqs. (8) and (9):

$$T_g(0, r) = T_{peak} \tag{14}$$

$$\frac{\partial T_g}{\partial r}(\hat{x}, r_o) = -H\left[T_g(\hat{x}, r_o) - T_{amb}\right] \tag{15}$$

$$\frac{\partial T_g}{\partial \hat{x}}(-\infty, r) = 0 \tag{16}$$

These boundary conditions and key assumptions are illustrated in Fig. 3. Equation (14) embeds the assumption that smouldering proceeded with constant intensity across the reactor radius. While constant peak temperatures are often observed in robust smouldering systems [22,23,26,27,33,57], the peak temperatures are generally cooler near the wall due to radial heat losses [58,74–76]. Furthermore, near-wall extinction (i.e., due to non-uniform reactions [51,58,64]) and airflow divergences (i.e., due to non-uniform air flux [58,74,75]) also lead to complicated dynamics. As non-uniform air flux and reactions were not critical to describe the evolution of E_{net}, they were not pursued. However, they are worthwhile to explore in multidimensional numerical models (e.g. Refs. [12,13,49,74,77]), as Rashwan et al. [26], demonstrated that they can lead to operational challenges, e.g., lower processing rates, peak temperatures, and heating rates.

Equation (15) describes the convective boundary at the edge of the insulation, where the temperature was assumed to decrease linearly across the thickness of the wrapped insulation. These assumptions are encapsulated in the modified heat transfer coefficient, $H = (k_{bulk} r_o [ln\{r_{o_{ins}}/r_o\}/k_{bulk_{ins}} + 1/h_{ins}\{r_{o_{ins}}\}])^{-1}$, where $r_{o_{ins}}$ is the outer radius of the insulation [29]. As the heat transfer coefficient (h_{ins}) at the outer radius of the insulation and the effective bulk conductivity of the insulation ($k_{bulk_{ins}}$) were unknown, H was varied as a bulk parameter in the sensitivity analysis in Section 3 (following [29]). Equation (16) assumes that the temperature did not vary axially far downstream of the smouldering front, which matches observations in long smouldering systems [48].

The boundary conditions in Eqs. 14–16 were then made non-dimensional using Eq. (10):

$$\theta_g(0, \xi_r) = 1 \tag{17}$$

$$\frac{\partial \theta_g}{\partial \xi_r}(\xi_x, R) = -\alpha_I \theta_g(\xi_x, R) \tag{18}$$

$$\frac{\partial \theta_g}{\partial \xi_x}(\infty, \xi_r) = 0 \tag{19}$$

where $R = r_o/r_o = 1$ and $\alpha_I = Hr_o$. Note that the sign of ∞ changed from Eqs. (16)–(19) because of the sign change in the axial transformation from $\hat{x}$ to ξ_x in Eq. (10).

With the boundary conditions in Eqs. 17–19, the analytical solution to Eq. (12) was achieved following the methodologies outlined in Refs. [70,78] (where additional insight can be found in Refs. [79,80]). The solution is therefore:

$$\theta_g(\xi_x, \xi_r) = \sum_{m=1}^{\infty} \frac{2\alpha_I R J_0\left(\frac{\xi_r \gamma_m}{R}\right)}{\left(\gamma_m^2 + \alpha_I^2 R^2\right) J_0(\gamma_m)} \times \exp\left\{\xi_x Pe_{eff}^2\left[\frac{1}{2} - \sqrt{\frac{1}{4} + \left(\frac{\gamma_m}{RPe_{eff}}\right)^2}\right]\right\} \tag{20}$$

where $J_1(\gamma_m) = \alpha_I R J_0(\gamma_m)$. The difference in phase temperatures, $\Delta\theta(\xi_x, \xi_r)$, was then solved using Eqs. (13) and (20):

$$\Delta\theta(\xi_x, \xi_r) = \sum_{m=1}^{\infty} \frac{2\alpha_I R J_0\left(\frac{\xi_r \gamma_m}{R}\right)}{\left(\gamma_m^2 + \alpha_I^2 R^2\right) J_0(\gamma_m)} \times \exp\left\{\xi_x Pe_{eff}^2\left[\frac{1}{2} - \sqrt{\frac{1}{4} + \left(\frac{\gamma_m}{RPe_{eff}}\right)^2}\right]\right\} \times \left\{Pe_{eff}^2(\lambda_I - \lambda_{II})\left[\frac{1}{2} - \sqrt{\frac{1}{4} + \left(\frac{\gamma_m}{RPe_{eff}}\right)^2}\right]\right\} \tag{21}$$

Altogether, Eqs. 20 and 21 are applicable to describe steady-state cooling zone temperatures across many applied smouldering systems with various fuels, fuel concentrations, air fluxes, reactor sizes, and insulation qualities. However, these systems need to facilitate sufficiently long and wide, reactionless cooling zones trailing a steady smouldering front (i.e., with constant peak temperatures and velocities) in systems with constant, uniform air fluxes and minimal LTNE. Therefore, Eqs. 20 and 21 cannot describe relatively short cooling zones in small radii reactors, or in systems that are highly affected by non-uniform air fluxes, reactions within the cooling zone, large temperature differences between phases, or any other dynamics beyond convective LTNE heat transfer.

2.3. Estimating $l_{cool,f}$ from a global energy balance

While Eqs. 20 and 21 provide descriptions of the gas and solid phase temperatures throughout the cooling-zone at steady-state conditions, Eqs. 22–24 provide a simplified description of the approximate final cooling zone length ($l_{cool,f}$) at the same conditions (i.e., when $\dot{E}_{oxid} \approx \dot{E}_{loss}$). This approximation was presented in Rashwan et al. [29], and is summarized below:

$$\dot{E}_{oxid} \approx \pi r_o^2 \Delta H_{oxid_{eff}} v_{oxid}(1-\varphi)\rho_s\left(\frac{m_{fuel}}{m_s}\right) \tag{22}$$

$$\dot{E}_{loss} \approx 2\pi r_o l_{cool,f} k_{bulk}\left(\frac{T_{peak} - T_{amb}}{2\left[\frac{x_c}{\alpha_{II}} + r_o\right]}\right) \tag{23}$$

$$l_{cool,f} \approx \frac{\Delta H_{oxid_{eff}} v_{oxid}(1-\varphi)\rho_s\left(\frac{m_{fuel}}{m_s}\right) r_o\left(\frac{x_c}{\alpha_{II}} + r_o\right)}{k_{bulk}\left(T_{peak} - T_{amb}\right)} \tag{24}$$

where $\Delta H_{oxid_{eff}}$ is the effective heat of smouldering (which accounts for pyrolysis and other endothermic processeslike water phase change), m_{fuel}/m_s is the mass ratio of fuel to sand, x_c is the characteristic heat transfer length from the convective-diffusive equation (i.e., $x_c = k_{bulk}/\rho_g C_{p_g} u_g$) [67], and α_{II} is the modified heat transfer coefficient used in Ref. [29] (i.e., $\alpha_{II} = Hx_c = \alpha_I x_c/r_o$).

2.4. Experimental and numerical results

The analyses from Sections 2.1-2.3 were applied to the data summarized in Table 1. DRUM R0-2, LAB R1-2, and LAB2 R0a-R0b were robust experiments that used granular activated carbon (GAC) in sand; LAB S1 used sewage sludge in sand; and LAB B1 simulated bitumen in sand using a 1D validated numerical model. The LAB experiments and LAB B1 used and simulated, respectively, reactors with 0.080 m radius – and the LAB2 and DRUM experiments used reactors with 0.054 and 0.300 m radii, respectively. See relevant schematics in the Supplementary Materials, Fig. S1.

Because all experiments and LAB B1 in Table 1 used and modelled, respectively, similar coarse grain sand, the same expressions for the air and sand thermophysical properties were used in the analyses in Sections 2.1-2.3. All effective thermophysical parameters were estimated over T_{amb} to T_{peak}, e.g., $\rho C_{p_{eff}} = \int_{T_{amb}}^{T_{peak}} \rho C_p(T) dT/(T_{peak} - T_{amb})$ [26,29,58]. See Table 2 for all parameters and references [27,56,60] for thorough descriptions of the parameter errors.

As noted in Table 1, all results have been detailed elsewhere, except LAB S1, which was an experiment with 72% MC sewage sludge mixed with coarse grain sand in a 1.135 m tall fuel bed. This experiment followed established experimental methods for conductive ignition [23, 26], and was instrumented with centreline thermocouples (spaced 0.02 m apart from 0.01 m below the heater to the top of the fuel bed) and continuous emissions analysis above the top of the pack (for O_2, CO_2, and CO). The same equipment detailed in Refs. [23,66] was used in this experiment (e.g., thermocouples, datalogger, insulation, conductive heater, coarse grain sand, source of sewage sludge). This experiment facilitated self-sustaining smouldering throughout most of the reactor but weakened and developed a large crust formation (further detailed below in Section 3). LAB S1 eventually quenched after smouldering 0.85 m. It is hypothesized that this quenching was due to water condensation and accumulation ahead of the smouldering front; this phenomena was observed in smouldering experiments using surrogate faeces under similar conditions [22]. Therefore, this experiment was analyzed prior to quenching when it achieved an approximately steady-state centreline temperature profile in the cooling zone. Note that these steady-state conditions are seldom observed in applied smouldering systems because they are often too short to allow cooling zone to fully develop – as it can grow multiple metres in robust systems based on common ranges of the terms in Eq. (24) [29]. All other experiments aside from LAB S1 in Table 1 reflect these typical smouldering conditions and were unsuitable for steady-state analyses. Therefore, LAB S1 provides unique and valuable experimental data to understand steady-state conditions within the cooling zone.

Table 2
Temperature-dependent model input parameters.

Par.	Details	Value[a]	Unit	Reference
T_{amb}	Varied between experiments	16–22	°C	[27,48, 73]
$\Delta H_{oxid_{eff}}$		0.98–25	MJ kg^{-1}	[29,48]
α_{II}	Used as a sensitivity parameter	0.1–1000	–	[29]
d_p	Constant in all experiments	2.00E-3	m	[29]
ρ_s		2650	kg m^{-3}	[29]
φ		0.37	–	[29]
σ		5.67E-8	W m^{-2} K^{-4}	[83]
k_p		8.0E-10	m^2	[58]
M		0.0290	kg mol^{-1}	[83]
R_g		8.31	m^3 Pa K^{-1} mol^{-1}	[83]
$C_{p_s}(T_s)$	$1.75T_s + 340.32$	1558	J kg^{-1} K^{-1}	[56]
$C_{p_g}(T_g)$	$-3\times10^{-5}(T_g^2) + 0.2261T_g + 940.35$	1081	J kg^{-1} K^{-1}	[56,83]
$\mu_g(T_g)$	$-9\times10^{-12}(T_g^2) + 4\times10^{-8}T_g + 6\times10^{-6}$	2.90E-5	Pa s	[56,83]
$k_{s_{app}}(T_s)$	$16\sigma d_p(T_s^3)/3 + 6.38\times10^{-4}T_s + 0.0915$	0.808	W m^{-1} K^{-1}	[56]
$k_g(T_g)$	$-1\times10^{-8}(T_g^2) + 8\times10^{-5}T_g + 4.3\times10^{-3}$	5.46E-2	W m^{-1} K^{-1}	[56,83]

[a] Average temperature dependent values are examples over the centreline T_{amb} to T_{peak} measured in DRUM R2.

2.5. Details on $\Delta H_{oxid_{eff}}$ estimations

The $\Delta H_{oxid_{eff}}$ values from DRUM R0-R2, LAB R1-R2, and LAB R0a-b (which used GAC) were estimated from the chemical equation: $C + (fr_{CO}/2 + [1 - fr_{CO}])O_2 \rightarrow 2fr_{CO}CO + (1 - fr_{CO})CO_2$ [58,60,74,75]. That is, the combustible fraction of GAC was assumed to be entirely carbon and degrade into CO and CO_2, and corrected for the GAC ash and moisture contents (see additional details and evidence in support of this procedure [27,60]). Therefore, 25 MJ kg^{-1} was used as $\Delta H_{oxid_{eff}}$ for DRUM R0-R2, LAB R1-R2, and LAB R0a-R0b based on the measured CO/CO_2 fractions [27,58,73]. 20 MJ kg^{-1} was used as the $\Delta H_{oxid_{eff}}$ for LAB B1, which accounted for the simulated exothermic and endothermic reactions from smouldering bitumen [48]. As the sewage sludge used in LAB S1 is a complex fuel that is influenced by many unresolved mass transfer processes and reactions, $\Delta H_{oxid_{eff}}$ could not be simply estimated from CO/CO_2 signals or from known heats of oxidation and pyrolysis. Instead, the heat of reaction on a dry mass basis ($\Delta H_{oxid,dry}$) for sewage sludge was estimated from Eq. (25):

$$(1 - MC_{crit})\Delta H_{oxid,dry} = MC_{crit}\Delta H_{vap} \quad (25)$$

where MC_{crit} is the critical moisture content that leads to quenching (i.e., observed experimentally as approximately 80% from Rashwan et al. [23]) and ΔH_{vap} is the heat of water vaporization from 25 °C (2.45 MJ kg^{-1}). Therefore, upon correcting for the MC in LAB S1 (i.e., 72%), the $\Delta H_{oxid_{eff}}$ for LAB S1 was estimated as 0.98 MJ kg^{-1} following:

$$\Delta H_{oxid_{eff}} = (1 - MC)\Delta H_{oxid,dry} - MC\Delta H_{vap} \quad (26)$$

Note that the energy balances in Eqs. 25 and 26 are highly simplified and a more rigorous analysis – if available – would be beneficial to estimate $\Delta H_{oxid_{eff}}$. However, the authors are not aware of a more reliable analysis with the data available from LAB S1. $\Delta H_{oxid_{eff}}$ is notoriously difficult to estimate in smouldering systems [27,46]. Therefore, in absence of an alternative analysis, Eqs. 25 and 26 provide a useful estimate of the energy released from LAB S1 to understand the steady-state conditions in that experiment.

2.6. Estimating $\overline{E}_{net}/A$ profiles from data

While the analyses outlined in Sections 2.1-2.3 provide a framework to fully describe the energy balance evolutions in smouldering systems, many smouldering studies only instrument or simulate the centreline ($r = 0$). Therefore, to compare with all data available in Table 1, only the centreline temperature data was used to define the stored energy per cross-sectional area along the centreline, E_{net}/A [27,29]:

$$\frac{E_{net}}{A} = \int_{x_0}^{x_f} \int_{T_{amb}}^{T_s(x,r=0,t)} (1 - \varphi)\rho_s C_{p_s}(T_s) dT dx \ : \ for\ 0 < t \quad (27)$$

where x_0 and x_f bound the fuel bed. The theoretical maximum stored

energy in the cooling zone, $E_{net,f}/A$, was estimated as:

$$\frac{E_{net,f}}{A} = \int_{-2l_{cool,f}}^{0} \int_{T_{amb}}^{T_s(x,r=0)} (1-\varphi)\rho_s C_{p_s} \left[(T_{peak} - T_{amb})\theta_s + T_{amb} \right] dT dx \quad (28)$$

where $\theta_s = \theta_g + \delta\Delta\theta$ is the solid phase temperature modelled along the system centreline from Eqs. 20 and 21 and $2l_{cool,f}$ from Eq. (24) was used as a practical boundary for Eq. (28) to delineate the end of the cooling zone; most of the cooling occurs between $0 \geq x \geq -l_{cool,f}$ but the integration in Eq. (28) was extended $-2l_{cool,f}$ to account for trailing temperatures (see an examples of $l_{cool,f}$ alongside analytical profiles in Fig. 5).

Following the results from Rashwan et al. [29], $\alpha_{II} = 0.5$ was used to estimate $E_{net,f}/A$ and t_f values for DRUM R0-R2 and LAB R1-R2. Moreover, because the LAB2 experiments from Zanoni et al. [73], used better quality insulation than DRUM R0-R2 and LAB R1-R2, $\alpha_{II} = 0.15$ was also used to estimate $E_{net,f}/A$ and t_f values for LAB2 R0a-b [65]. The respective reactor radii were used as the r_o terms for all analyses, except for LAB S1. LAB S1 exhibited a restricted effective radius due to a large crust formation; therefore, $\alpha_{II} = 100$ and $r_o = 0.055$ m were used to estimate $E_{net,f}/A$ and t_f from that experiment (see justification below in Section 3). The E_{net}/A measured when the heater was turned off ($t = t_{ig}$) was used as $E_{net,ig}/A$ in all analyses. To make the results from LAB B1 non-dimensional: the final E_{net}/A measurement was used as $E_{net,f}/A$ (i.e., from the maximum E_{net} value in Fig. 2c) and t_f was estimated with Eq. (3) – like the experimental data – except $\dot{E}_{loss}$ was calculated using the modelling conditions from Zanoni et al., [48]. That is, $k_{bulk}/([x_c/\alpha_{II}]+r_o)$ in Eq. (23) was substituted with the global heat loss parameter used in the LAB B1 simulation, i.e., $U = 13$ W m^2 K^{-1} [56].

Though $E_{net,f}/A$ accounted for most of the stored energy in the systems (i.e., in the cooling zone), it did not account for the small amount of energy stored in the reaction and preheating zones (Fig. 1), which were captured in E_{net}/A values – see Eq. (27). Therefore, at near steady-state conditions, E_{net}/A is larger than $E_{net,f}/A$. Altogether, many simplifying assumptions were used to approximate $E_{net,f}/A$ and t_f, which are therefore imperfect but useful. Regardless of the limitations, the key energy balance trends can be identified by making E_{net}/A profiles non-dimensional following:

$$\frac{\overline{E}_{net}}{A} = \frac{\frac{E_{net}}{A} - \frac{E_{net,ig}}{A}}{\frac{E_{net,f}}{A} - \frac{E_{net,ig}}{A}} \quad (29)$$

The non-dimensional energy profile ($\overline{E}_{net}/A$) can then be evaluated from various data sources and compared together.

3. Results and discussion

Fig. 4 compares centreline temperature spatial profiles from three example experiments (DRUM R2, LAB R2, and LAB S1 in Fig. 4b, c, and d, respectively) alongside a theoretical adiabatic profile in Fig. 4a. The temperatures were made non-dimensional following Eq. (10) and the distances were normalized to the cooling zone length (l_{cool}) at each snapshot in time. The data from DRUM R2 and LAB R2 were gathered near the end of smouldering, i.e., when the smouldering front was near the end of the fuel bed (x_f) respective to each system, and from LAB S1 after steady-state conditions were reached ($\tau > 1$). Note that the temperature markers in Fig. 4d ahead of smouldering (i.e., righthand side) are not at ambient values because of evaporation and recondensation of the wet sewage sludge [54]. The sizes of the smouldering and cooling velocity vectors (v_{oxid} and v_{cool}, respectively) indicate their relative speeds.

The $\overline{E}_{net}/A$ values in: (*i*) Fig. 4a is a theoretical minimum in an adiabatic system; (*ii*) Fig. 4b–c were the maximum values measured; and (*iii*) Fig. 4d is a theoretical maximum in a steady-state system, which was close to the $\overline{E}_{net}/A$ values measured (see LAB S1's $\overline{E}_{net}/A$ profile in Fig. 7). Fig. 4 also illustrates the centreline temperature profile corresponding to changes in $\overline{E}_{net}/A$. Fig. 4a shows a theoretical condition where all energy generated is stored in the system. In this case, $\overline{E}_{net}/A = 0$ because $E_{net,f}/A$ tends to infinity in an adiabatic system, as the cooling length grows unboundedly – see Eq. (29). Fig. 4b shows the temperatures from DRUM R2, which was an experiment that smouldered GAC in a large reactor (0.3 m radius) with minimal heat losses relative to the energy released after propagating 0.8 m with $\overline{E}_{net}/A \approx 0.1$. Fig. 4c shows the temperatures from LAB R2, which was an experiment that followed the same conditions as DRUM R2 but in a small reactor (0.08 m radius), after propagating 0.5 m, where $\overline{E}_{net}/A \approx 0.4$. In other words, the increase in $\overline{E}_{net}/A$ from Fig. 4b to c indicate the increased influence of heat losses due to the decreasing reactor radii [27,29]. Fig. 4d shows a key limiting case from LAB S1 after propagating 0.5 m with $\overline{E}_{net}/A \approx 1$. This high $\overline{E}_{net}/A$ value indicates that the stored energy was near the system's maximum value when $\dot{E}_{loss}$ and $\dot{E}_{oxid}$ roughly balance – see Eq. (1). Note that the $l_{cool}(t)$ values on Fig. 4a–c were transient and grew throughout propagation, as $v_{oxid} > v_{cool}$ [29,60]. In these frames, v_{cool} was controlled by the axial heat transfer, i.e., $v_{cool} = \rho_g C_{p_g} u_g / (\rho C_p)_{bulk}$ [67]. On the other hand, the cooling zone length in the steady-state condition

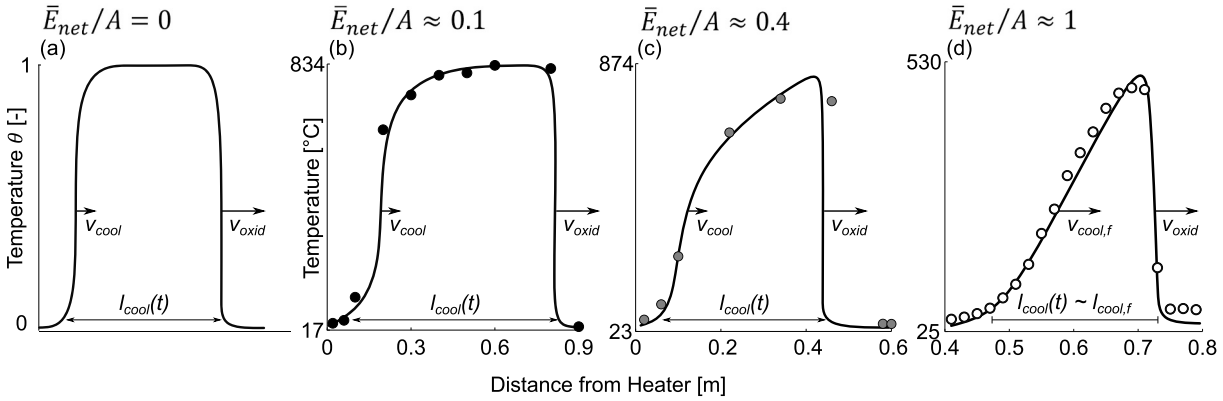

Fig. 4. (a–d) Conceptual models (solid lines) of the centreline spatial temperature profiles transitioning from (a) adiabatic ($\overline{E}_{net}/A = 0$) to (d) approximately steady-state conditions ($\overline{E}_{net}/A = 1$) when the energy released rate from smouldering approximately equals the heat loss rate from the system, i.e., $\dot{E}_{oxid} \approx \dot{E}_{loss}$. The overlain data markers are from snapshots from select experiments that demonstrate this transition. The black, grey, and white markers in (b), (c), and (d), respectively, are the centreline temperature profiles from DRUM R2, LAB R2, and LAB S1, respectively (see Table 1). The net stored energy along the centreline ($\overline{E}_{net}/A$), smouldering velocities (v_{oxid}), cooling velocities (v_{cool}), and cooling zone lengths (l_{cool}) are labelled for further discussion in the text; note that the maximum final cooling zone length and cooling velocity are $l_{cool,f}$ and $v_{cool,f}$, respectively.

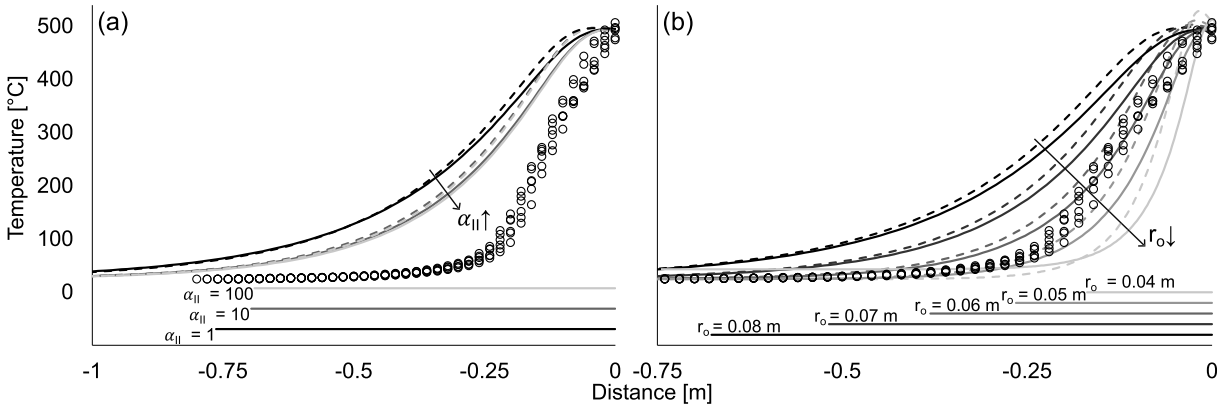

Fig. 5. (a) and (b) cooling zone temperature data from LAB S1 (circles) compared to the modelled sand (dashed lines) and air (solid lines) temperatures from Eqs. 20 and 21 under various model assumptions. The origin in (a) and (b) is anchored to the peak temperature observed as the smouldering front, and the negative coordinates indicate the cooling zone behind the smouldering front. The straight lines underneath the analytical curves indicated the maximum cooling zone lengths, i.e., $l_{cool,f}$ from Eq. (24), at the same conditions as the analytical curves. The sensitivities to insulation quality (α_{II}) and reactor radius (r_o) are overlain to (a) and (b), respectively. Note that $r_o = 0.08$ m and $\alpha_{II} = 100$ in (a) and (b), respectively, and the $\alpha_{II} = 10$ and $\alpha_{II} = 100$ curves are nearly overlain in (a).

in Fig. 4d was constant at a maximum value, i.e., $l_{cool,f}$, which can be estimated from Eq. (24). Moreover, the cooling velocity in this condition ($v_{cool,f}$) was also a maximum value and controlled by perimeter heat losses, where $v_{cool,f} \approx v_{oxid}$. Altogether, Fig. 4 illustrates the characteristic evolution of spatial temperature profiles in applied smouldering systems, from adiabatic ($\bar{E}_{net}/A = 0$) to steady-state ($\bar{E}_{net}/A \approx 1$) conditions.

Fig. 5a–b compares temperatures measured from LAB S1 with those modelled with Eqs. 20–24 to build confidence in the model formulation, where solid and dashed lines indicated air and sand temperatures, respectively. The temperature measurements (circles) were taken when the smouldering front travelled 0.71–0.81 m, as identified via the peak temperatures over this period, which averaged 496 °C. This timeframe was chosen so to show a wide spread of the trailing cooling zone temperatures that were well-within LAB S1's late-time period (i.e., $\tau > 1$), which occurred after the smouldering front travelled approximately 0.26 m. The smouldering front was anchored at $x = 0$ m in Fig. 5a–b to compare with Eqs. 20 and 21. Note that the steady-state cooling lengths ($l_{cool,f}$) from Eq. (24) were compared alongside the modelled temperatures at corresponding model conditions (i.e., horizontal lines below the temperatures). Sensitivity analyses were completed on the insulation quality (α_{II}) and the outer radius (r_0) to explore the influence of these key system parameters, and better understand the consequences of the crust formation in LAB S1. Fig. 6 is a top-down photo of the cross-section from LAB S1 upon excavation.

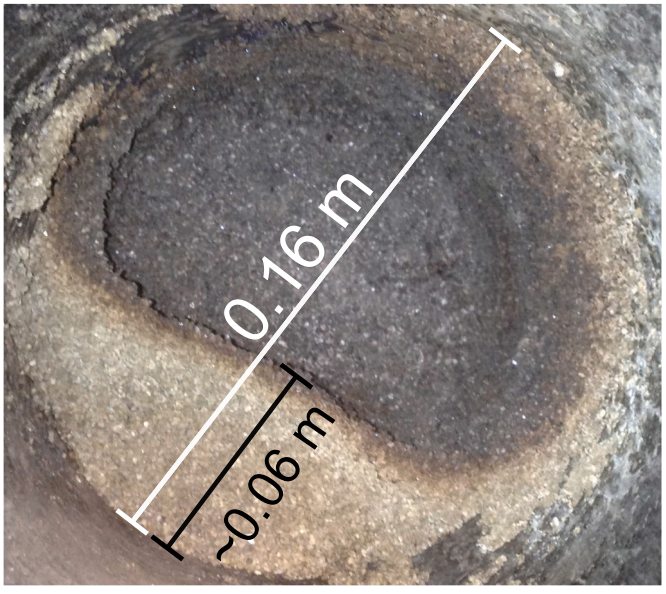

Fig. 6. A photo of the crust from LAB S1 with dimensions labelled.

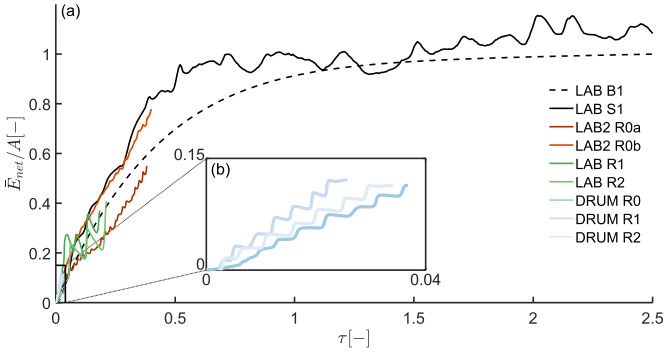

Fig. 7. (a) The non-dimensional energy per area and time results from all data in Table 1. Only every tenth data point from the experimental results (solid lines) were plotted for clarity. All data points from the simulation LAB B1 (dashed line) were plotted. (b) The inset isolates the profiles from DRUM R0-R2.

Fig. 5a shows the small influence of α_{II} from 1 to 100 on the temperatures with $r_0 = 0.08$ m. This insensitivity indicates that when the insulation is poor, it effectively leads to a constant temperature condition at the outer radius, i.e., heat transfer out of the insulation is fast and the outer-radius remains near T_{amb} (see Supplementary Materials, Fig. S2). This range of poor insulation (i.e., high α_{II} values) was explored to approximate the effects of a crust formed near the wall from LAB S1. As shown in Fig. 6, LAB S1 exhibited a large, unburned ring of crust. This crust drew large heat losses that were not explicitly modelled, only approximated with high α_{II} values.

While the model results in Fig. 5a do not match with experimental measurements, Fig. 5b shows much better matching by decreasing r_0 with $\alpha_{II} = 100$. Though LAB S1 was performed in a 0.08 m radius reactor, Fig. 6 shows that the unburned edge grew non-uniformly inward, which effectively reduced the radius for smouldering and energy storage in the cooling zone. From the sensitivity analysis in Fig. 5b, the modelled temperatures with an effective radius near 0.05–0.06 m best captured the observed temperatures, which approximately match the observed crust growth in Fig. 6. Therefore, $r_o = 0.055$ m was used to estimate t_f and $E_{net,f}/A$ from LAB S1. In Fig. 5a–b, the overlain sand and

air temperatures show comparable differences as previous perturbation analyses with similar analytical models [26,29,58]. In Fig. 5a–b, these temperature differences increase as α_{II} increases and r_o decreases, which indicates that phase temperature differences dampen in long cooling zones with gradual temperature gradients. Moreover, the elevated solid temperatures near $x = 0$ m at small radii in Fig. 5b were due to solution instabilities, e.g., most noticeable with $r_o = 0.04$ m. The perturbation model is least reliable at small radii (as discussed in Section 2.2). Moreover, the $l_{cool,f}$ values in Fig. 5a–b approximately captured the cooling zone lengths of the modelled temperature profiles. Altogether, Fig. 5 illustrates that the model assumptions embedded Eqs. 20–24 provide valuable insight into applied smouldering systems' cooling zones at steady-state conditions.

Fig. 7 illustrates the $\overline{E}_{net}/A$ profiles during smouldering from all models and experiments in Table 1 over non-dimensional time (τ) via the methods summarized in Section 2. Note that no experimental curve perfectly approaches $\overline{E}_{net}/A \rightarrow 1$ because many simplifying assumptions were needed to harmonize the data (see details in Section 2). Moreover, the experimental curves exhibit false oscillations, which were primarily due to coarse thermocouple placements [27]. As an exception, the LAB B1 exhibits a smooth curve and does reach $\overline{E}_{net}/A = 1$ at $\tau = 2.4$, as the maximum E_{net}/A value modelled was used as $E_{net,f}/A$ (see details in Section 2.6). Most importantly, all $\overline{E}_{net}/A$ profiles generally collapse onto each other; therefore, Fig. 7 illustrates that the assumptions used throughout the analyses in Section 2 do successfully clarify the non-dimensional, characteristic energy balance evolution of applied smouldering systems.

As discussed throughout this manuscript, the experiments and models exhibited many differences; however, the implications of these differences on their global energy balances can be distilled in the extent of their $\overline{E}_{net}/A$ profiles. That is, DRUM R0-R2 show relatively short profiles in Fig. 7 that progress until $\overline{E}_{net}/A \approx 0.1$, $\tau \approx 0.03-0.04$ (see the inset in Fig. 7b for clarity). These short profiles illustrate that DRUM R0-R2 operated only in early durations of the characteristic energy curve. In other words, the global energy balances from Eq. (1) in DRUM R0-R2 were far from steady-state conditions and these experiments accumulated large amounts of released reaction energy throughout their operation. Conversely, the other experiments and simulations in Fig. 7 exhibited longer profiles than the DRUM experiments. For example, the profiles from LAB R1-R2 and LAB2 R0a-R0b were longer as they used smaller radii (i.e., DRUM: 0.300 m, LAB: 0.080 m, and LAB2: 0.054 m) at similar smouldering conditions (e.g., fuel type, concentration, and applied air flux – see Table 1). The decreasing reactor radii promoted greater relative heat losses, which drove the global energy balances in LAB R1-R2 and LAB2 R0a-R0b closer toward steady-state conditions [27,29]. The simulation LAB B1 and experiment LAB S1 both exhibited the longest profiles on Fig. 7, which approached $\overline{E}_{net}/A \rightarrow 1$. LAB B1 and S1 demonstrate global energy balance evolutions towards steady-state conditions when the rate of heat losses ($\dot{E}_{loss}$) approximately balance the rate of energy released from exothermic smouldering reactions ($\dot{E}_{oxid}$). While Zanoni et al. [48], demonstrated this evolution numerically under specific conditions in Fig. 2, this study identifies the key parameters that govern this transition generally. Altogether, Fig. 7 demonstrates the characteristic global energy balance evolution in applied smouldering systems, which can be manipulated by engineers to better design future systems.

4. Conclusions

Under a broad range of experimental and modelling conditions, the global energy balance evolutions in applied smouldering systems have been examined and a unified, characteristic profile has been elucidated. This characteristic profile was uncovered through using a description of the global energy balance at steady-state conditions, i.e., when the rate of energy released from smouldering approximately balanced perimeter heat losses. This analysis exploited the fact that most stored energy in applied smouldering systems accumulate within the cooling zone. Therefore, a new analytical description of cooling zone steady-state temperature distribution was used to estimate the maximum stored energy, and the cooling and smouldering velocities were used to approximate the time needed to reach these conditions.

Altogether, this study provides novel insight into the key drivers that govern the characteristic energy distribution and evolution in applied smouldering systems, which can be manipulated by engineers and researchers to design improved applied smouldering systems.

Credit author statement

Tarek L. Rashwan: Conceptualization, Data curation, Software, Formal analysis, Funding acquisition, Investigation, Methodology, Project administration, Validation, Visualization, Writing – original draft; **Marco A. B. Zanoni**: Data curation, Investigation, Methodology, Visualization, Writing – review & editing; **Jiahao Wang**: Data curation, Investigation, Methodology, Writing – review & editing; **José L. Torero**: Conceptualization, Formal analysis, Investigation, Methodology, Supervision, Project administration, Resources, Writing – review & editing; **Jason I. Gerhard**: Conceptualization, Funding acquisition, Methodology, Project administration, Resources, Supervision, Writing – review & editing.

Declaration of competing interest

The authors declare that they have no known competing financial interests or personal relationships that could have appeared to influence the work reported in this paper.

Data availability

Data will be made available on request.

Acknowledgements

Funding was provided by the Ontario Ministry of Research, Innovation, and Science; the Government of Canada through the Federal Economic Development Agency for Ontario through the Ontario Water Consortium's Advancing Water Technologies Program (Grant SUB02392) with in-kind support from: (*i*) the Ontario Ministry of the Environment, Conservation and Parks and (*ii*) Savron (a wholly owned subdivision of Geosyntec Consultants Ltd); the Natural Sciences and Engineering Research Council of Canada (Postgraduate Scholarship-Doctoral PGSD3 - 489978–2016 and Grant Nos. CREATE 449311–14, RGPIN 2018–06464, and RGPAS-2018-522602); the Water Environment Association of Ontario's Residuals and Biosolids Research Fund Award (2018 and 2019); a 2022-23 Higher Education Innovation Funding Knowledge Transfer Voucher from The Open University; and a travel stipend to the first author from the Remediation Education Network Program. We gratefully acknowledge additional project support from Gudgeon Thermfire International (especially from Justin Barfett and Randy Adamski), London Ontario's Greenway Wastewater Treatment Centre (especially from Randy Bartholomew, Michael Wemyss, and Anthony Van Rossum), Dr. Taryn Fournie, Dr. Gavin Grant, Joshua Brown, Cody Murray, Zia Miry, Megan Green, Anna Toner, Brendan Evers, Thomas Mathias, Dillon McIntyre, Jordan Teeple, Jad Choujaa, Maxwell Servos, Reid Clementino, Kia Barrow, Nick Rogowski, and Christopher Kwan. Most importantly, this paper is dedicated in loving memory of our colleague, mentor, and dear friend, Dr. Jason Gerhard.

Appendix A. Supplementary data

Supplementary data to this article can be found online at https://doi.

org/10.1016/j.energy.2023.127245.

References

[1] Grant GP, Major D, Scholes GC, Horst J, Hill S, Klemmer MR, Couch JN. Smoldering combustion (STAR) for the treatment of contaminated soils: examining limitations and defining success. Remed J 2016;26(3):27–51.
[2] Vidonish JE, Zygourakis K, Masiello CA, Sabadell G, Alvarez PJJ. Thermal treatment of hydrocarbon-impacted soils: a review of technology innovation for sustainable remediation. Engineering 2016;2(4):426–37.
[3] Zhao C, Li Y, Gan Z, Nie M. Method of smoldering combustion for refinery oil sludge treatment. J Hazard Mater 2021;409:124995.
[4] Gan Z, Zhao C, Li Y, Chen G, Song Z, Zhang Z, Ran W. Experimental investigation on smoldering combustion for oil sludge treatment: influence of key parameters and product analysis. Fuel 2022;316:123354.
[5] Wyn HK, Konarova M, Beltramini J, Perkins G, Yermán L. Self-sustaining smouldering combustion of waste: a review on applications, key parameters and potential resource recovery. Fuel Process Technol 2020;205:106425.
[6] Manelis GB, Glazov SV, Salgansky EA, Lempert DB, Gudkova IY, Domashnev IA, Kolesnikova AM, Kislov VM, Kolesnikova YY. Extraction of molybdenum-containing species from heavy oil residues using the filtration combustion method. Int J Heat Mass Tran 2016;92:744–50.
[7] Fournie T, Rashwan TL, Switzer C, Gerhard JI. Phosphorus recovery and reuse potential from smouldered sewage sludge ash. Waste Manag 2022;137:241–52.
[8] Ezieke AH, Serrano A, Clarke W, Villa-Gomez DK. Bottom ash from smouldered digestate and coconut coir as an alkalinity supplement for the anaerobic digestion of fruit waste. Chemosphere 2022;296:134049.
[9] Yan S, Yin D, He F, Cai J, Schliermann T, Behrendt F. Characteristics of smoldering on moist rice husk for silica production. Sustainability 2022;14(1):317.
[10] Duque JVF, Bittencourt FLF, Martins MF, Debenest G. Developing a combustion-driven reactor for waste conversion. Energy 2021:121489.
[11] Wyn HK, Zárate S, Carrascal J, Yermán L. A novel approach to the production of biochar with improved fuel characteristics from biomass waste. Waste Biomass Valorization; 2019.
[12] Pan R, Debenest G. Numerical investigation of a novel smoldering-driven reactor for plastic waste pyrolysis. Energy Convers Manag 2022;257:115439.
[13] Pan R, Debenest G, Zanoni MAB. A robust two-dimensional model for the pyrolysis of plastic waste driven by self-sustaining smoldering. Process Saf Environ Protect 2022;162:610–9.
[14] Bittencourt FLF, Martins MF, Orlando MTD, Galvão ES. The proof-of-concept of a novel feces destroyer latrine. J Environ Chem Eng 2022;10(1):106827.
[15] Somorin TO. Valorisation of human excreta for recovery of energy and high-value products: a mini-review. In: Daramola MO, Ayeni AO, editors. Valorization of biomass to value-added commodities: current trends, challenges, and future prospects. Cham: Springer International Publishing; 2020. p. 341–70.
[16] Song Z, He T, Li M, Wu D, You F. Self-sustaining smoldering as a novel disposal approach for food waste with high moisture content. Fuel Process Technol 2022; 228:107144.
[17] Feng C, Cheng M, Gao X, Qiao Y, Xu M. Occurrence forms and leachability of inorganic species in ash residues from self-sustaining smouldering combustion of sewage sludge. Proc Combust Inst 2021;38(3):4327–34.
[18] Feng C, Huang J, Yang C, Li C, Luo X, Gao X, Qiao Y. Smouldering combustion of sewage sludge: volumetric scale-up, product characterization, and economic analysis. Fuel 2021;305:121485.
[19] Cheng S, Gao X, Cao L, Wang Q, Qiao Y. Quantification of total organic carbon in ashes from smoldering combustion of sewage sludge via a thermal treatment—TGA method. ACS Omega 2020;5(51):33445–54.
[20] Pironi P, Switzer C, Gerhard JI, Rein G, Torero JL. Self-sustaining smoldering combustion for NAPL remediation: laboratory evaluation of process sensitivity to key parameters. Environ Sci Technol 2011;45(7):2980–6.
[21] Switzer C, Pironi P, Gerhard J, Rein G, Torero J. Self-sustaining smoldering combustion: a novel remediation process for non-aqueous-phase liquids in porous media. Environ Sci Technol 2009;43(15):5871–7.
[22] Yermán L, Hadden RM, Carrascal J, Fabris I, Cormier D, Torero JL, Gerhard JI, Krajcovic M, Pironi P, Cheng Y-L. Smouldering combustion as a treatment technology for faeces: exploring the parameter space. Fuel 2015;147:108–16.
[23] Rashwan TL, Gerhard JI, Grant GP. Application of self-sustaining smouldering combustion for the destruction of wastewater biosolids. Waste Manag 2016;50: 201–12.
[24] Serrano A, Wyn H, Dupont L, Villa-Gomez DK, Yermán L. Self-sustaining treatment as a novel alternative for the stabilization of anaerobic digestate. J Environ Manag 2020;264:110544.
[25] Vantelon J-P, Lodeho B, Pignoux S, Ellzey JL, Torero JL. Experimental observations on the thermal degradation of a porous bed of tires. Proc Combust Inst 2005;30(2): 2239–46.
[26] Rashwan TL, Fournie T, Torero JL, Grant GP, Gerhard JI. Scaling up self-sustained smouldering of sewage sludge for waste-to-energy. Waste Manag 2021;135: 298–308.
[27] Rashwan TL, Torero JL, Gerhard JI. The improved energy efficiency of applied smouldering systems with increasing scale. Int J Heat Mass Tran 2021;177:121548.
[28] Scholes GC, Gerhard JI, Grant GP, Major DW, Vidumsky JE, Switzer C, Torero JL. Smoldering remediation of coal-tar-contaminated soil: pilot field tests of STAR. Environ Sci Technol 2015;49(24):14334–42.
[29] Rashwan TL, Torero JL, Gerhard JI. Heat losses in applied smouldering systems: sensitivity analysis via analytical modelling. Int J Heat Mass Tran 2021;172: 121150.
[30] Gerhard JI, Grant GP, Torero JL. Chapter 9 - star: a uniquely sustainable in situ and ex situ remediation process. In: Hou D, editor. Sustainable remediation of contaminated soil and groundwater. Butterworth-Heinemann; 2020. p. 221–46.
[31] Solinger R, Grant GP, Scholes GC, Murray C, Gerhard JI. STARx Hottpad for smoldering treatment of waste oil sludge: proof of concept and sensitivity to key design parameters. Waste Manag Res 2020;38(5):554–66.
[32] Morales RB, DeGroot CT, Scholes GC, Gerhard JI. Understanding, controlling and optimising the cooling of waste thermal treatment beds including STARx Hottpads. Waste Manag Res 2022:0734242X221076308.
[33] Fabris I, Cormier D, Gerhard JI, Bartczak T, Kortschot M, Torero JL, Cheng Y-L. Continuous, self-sustaining smouldering destruction of simulated faeces. Fuel 2017;190:58–66.
[34] Salgansky EA, Zaichenko AY, Podlesniy DN, Salganskaya MV, Tsvetkov MV, Chub AV. Gasification of oil shale dust in a counterflow moving bed filtration combustion reactor. Int J Hydrogen Energy 2020;45(35):17270–5.
[35] Podlesniy D, Zaichenko A, Tsvetkov M, Salganskaya M, Chub A, Salgansky E. Experimental investigation of waste oil processing by partial oxidation in a moving bed reactor. Fuel 2021;298:120862.
[36] Ma L, Yan C, Feng C, Qiao Y, Huang J, Fang Q, et al. Experimental investigation on self-sustained smouldering of food-processing sludge with extremely high moisture content: from laboratory-scale to pilot-scale volumetric scale-up. Waste Manag 2023;158:13–22.
[37] Pape A, Switzer C, McCosh N, Knapp CW. Impacts of thermal and smouldering remediation on plant growth and soil ecology. Geoderma 2015;243:1–9.
[38] Zihms SG, Switzer C, Irvine J, Karstunen M. Effects of high temperature processes on physical properties of silica sand. Eng Geol 2013;164:139–45.
[39] Chen Y, Lin S, Liang Z, Surawski NC, Huang X. Smouldering organic waste removal technology with smoke emissions cleaned by self-sustained flame. J Clean Prod 2022;362:132363.
[40] Fournie T, Rashwan TL, Switzer C, Grant GP, Gerhard JI. Exploring PCDD/Fs and potentially toxic elements in sewage sludge during smouldering treatment. J Environ Manag 2022;317:115384.
[41] Chen Y, Lin S, Liang Z, Huang X. Clean smoldering biowaste process: effect of burning direction on smoke purification by self-sustained flame. Fuel Process Technol 2022;237:107453.
[42] Duque JVF, Martins MF, Bittencourt FLF, Debenest G. Relevant aspects of propagating a combustion front in an annular reactor for out-of-bed heat recovery. Exp Therm Fluid Sci 2022;133:110575.
[43] Bittencourt FLF, Debenest G, Martins MF. Free convection development caused by bed shrinkage in a vacuum-induced smoldering reactor. Chem Eng J 2021:132847.
[44] Deng J, Zhou F, Shi B, Torero JL, Qi H, Liu P, Ge S, Wang Z, Chen C. Waste heat recovery, utilization and evaluation of coalfield fire applying heat pipe combined thermoelectric generator in Xinjiang, China. Energy 2020;207:118303.
[45] Shi B, Su H, Li J, Qi H, Zhou F, Torero JL, Chen Z. Clean power generation from the intractable natural coalfield fires: turn harm into benefit. Sci Rep 2017;7(1):5302.
[46] Torero JL, Gerhard JI, Martins MF, Zanoni MAB, Rashwan TL, Brown JK. Processes defining smouldering combustion: integrated review and synthesis. Prog Energy Combust Sci 2020;81:100869.
[47] Ohlemiller TJ. Modeling of smoldering combustion propagation. Prog Energy Combust Sci 1985;11(4):277–310.
[48] Zanoni MAB, Torero JL, Gerhard JI. Determining the conditions that lead to self-sustained smouldering combustion by means of numerical modelling. Proc Combust Inst 2019;37(3):4043–51.
[49] Lin S, Yuan H, Huang X. A computational study on the quenching and near-limit propagation of smoldering combustion. Combust Flame 2022;238:111937.
[50] Lu Z. Structure and extinction of reverse smolder waves in the presence of heat losses: a premixed-flame perspective. Combust Flame 2022;242:112201.
[51] Pironi P, Switzer C, Rein G, Fuentes A, Gerhard JI, Torero JL. Small-scale forward smouldering experiments for remediation of coal tar in inert media. Proc Combust Inst 2009;32(2):1957–64.
[52] Zanoni MAB, Rein G, Yermán L, Gerhard JI. Thermal and oxidative decomposition of bitumen at the Microscale: kinetic inverse modelling. Fuel 2020;264:116704.
[53] Hadden RM, Rein G, Belcher CM. Study of the competing chemical reactions in the initiation and spread of smouldering combustion in peat. Proc Combust Inst 2013; 34(2):2547–53.
[54] Zanoni MAB, Wang J, Torero JL, Gerhard JI. Multiphase modelling of water evaporation and condensation in an air-heated porous medium. Appl Therm Eng 2022:118516.
[55] Lin S, Huang X. Quenching of smoldering: effect of wall cooling on extinction. Proc Combust Inst 2021;38(3):5015–22.
[56] Zanoni MAB, Torero JL, Gerhard JI. Determination of the interfacial heat transfer coefficient between forced air and sand at Reynold's numbers relevant to smouldering combustion. Int J Heat Mass Tran 2017;114(Supplement C):90–104.
[57] Zanoni MAB, Torero JL, Gerhard JI. The role of local thermal non-equilibrium in modelling smouldering combustion of organic liquids. Proc Combust Inst 2019;37 (3):3109–17.
[58] Rashwan TL, Torero JL, Gerhard JI. Heat losses in a smouldering system: the key role of non-uniform air flux. Combust Flame 2021;227:309–21.
[59] Zanoni MAB, Torero JL, Gerhard JI. Delineating and explaining the limits of self-sustained smouldering combustion. Combust Flame 2019;201:78–92.
[60] Rashwan TL. Sustainable smouldering for waste-to-energy: scale, heat losses, and energy efficiency [PhD]. London, Canada: The University of Western Ontario; 2020.

[61] Dosanjh SS, Pagni PJ, Fernandez-Pello AC. Forced cocurrent smoldering combustion. Combust Flame 1987;68(2):131–42.
[62] Aldushin AP, Rumanov IE, Matkowsky BJ. Maximal energy accumulation in a superadiabatic filtration combustion wave. Combust Flame 1999;118(1–2):76–90.
[63] Liu L, Pang Y, Lv D, Wang K, Wang Y. Self-sustaining smoldering characteristics of corn straw powder stacks. ACS Omega 2021;6(14):9928–39.
[64] Zanoni MAB, Torero JL, Gerhard JI. Experimental and numerical investigation of weak, self-sustained conditions in engineered smouldering combustion. Combust Flame 2020;222:27–35.
[65] Miry SZ, Zanoni MAB, Rashwan TL, Torero JL, Gerhard JI. Investigation of multi-dimensional transfer effects in applied smouldering systems: a 2D numerical modelling approach. Combust Flame 2022;246:112385.
[66] Kinsman L, Torero JL, Gerhard JI. Organic liquid mobility induced by smoldering remediation. J Hazard Mater 2017;325:101–12.
[67] Kuznetsov AV. An investigation of a wave of temperature difference between solid and fluid phases in a porous packed bed. Int J Heat Mass Tran 1994;37(18):3030–3.
[68] Kuznetsov AV. Thermal nonequilibrium forced convection in porous media. In: Ingham DB, Pop I, editors. Transport phenomena in porous media. Oxford: Pergamon; 1998. p. 103–29.
[69] Torero J, Fernandez-Pello A. Forward smolder of polyurethane foam in a forced air flow. Combust Flame 1996;106(1):89–109.
[70] Kuznetsov AV. Investigation of a non-thermal equilibrium flow of an incompressible fluid in a cylindrical tube filled with porous media. ZAMM-Z Angew Math Me. 1996;76(7):411–8.
[71] Dixon AG, Cresswell DL. Theoretical prediction of effective heat transfer parameters in packed beds. AIChE J 1979;25(4):663–76.
[72] Wakao N, Kaguei S, Funazkri T. Effect of fluid dispersion coefficients on particle-to-fluid heat transfer coefficients in packed beds: correlation of nusselt numbers. Chem Eng Sci 1979;34(3):325–36.
[73] Zanoni MAB, Wang J, Gerhard JI. Understanding pressure changes in smouldering thermal porous media reactors. Chem Eng J 2021;412:128642.
[74] Pozzobon V, Baud G, Salvador S, Debenest G. Darcy scale modeling of smoldering: impact of heat loss. Combust Sci Technol 2017;189(2):340–65.
[75] Martins MF, Salvador S, Thovert JF, Debenest G. Co-current combustion of oil shale – Part 2: structure of the combustion front. Fuel 2010;89(1):133–43.
[76] Baud G, Salvador S, Debenest G, Thovert J-F. New granular model medium to investigate smoldering fronts propagation—experiments. Energy Fuel 2015;29(10):6780–92.
[77] Lutsenko NA. Numerical model of two-dimensional heterogeneous combustion in porous media under natural convection or forced filtration. Combust Theor Model 2018;22(2):359–77.
[78] Vick B, Özişik MN. Effects of axial conduction and convective boundary conditions in slug flow inside a circular tube. J Heat Tran 1981;103(3):436–40.
[79] Özışık MN. Heat conduction. John Wiley & Sons; 1993.
[80] Carslaw HS, Jaeger JC. Conduction of heat in solids. second ed. Oxford: Clarendon Press; 1959.
[81] Salman M, Gerhard JI, Major DW, Pironi P, Hadden R. Remediation of trichloroethylene-contaminated soils by star technology using vegetable oil smoldering. J Hazard Mater 2015;285:346–55.
[82] Duchesne AL, Brown JK, Patch DJ, Major D, Weber KP, Gerhard JI. Remediation of PFAS-contaminated soil and granular activated carbon by smoldering combustion. Environ Sci Technol 2020;54(19):12631–40.
[83] Bergman TL, Lavine AS, Incropera FP, DeWitt DP. Fundamentals of heat and mass transfer. seventh ed. New York, NY: John Wiley & Sons; 2011.